npj | flexible electronics

Article

Published in partnership with Nanjing Tech University

https://doi.org/10.1038/s41528-025-00489-2

Integrated health monitoring system with flexible asymmetric supercapacitors based on 2D Ti_3C_2 MXene and transitional metal oxides

Kaaviah Manoharan[1] & Martin Pumera[1,2,3,4]

Developing flexible, lightweight, and portable medical devices for continuous health monitoring requires compact and sustainable energy storage solutions. Traditional devices often rely on bulky wired equipment or battery-powered systems requiring frequent recharging, limiting practicality. We developed a flexible and stable asymmetric supercapacitor using MXene and transition metal oxide nanocomposite. In half cells, the electrolyte was 1M H_2SO_4; in full cells, a PVA/H_2SO_4 gel was used. Among the composites, $Fe_2O_3@Ti_3C_2$ showed superior electrochemical performance due to surface redox reactions enhancing pseudocapacitance. The $Fe_2O_3@Ti_3C_2||Ti_3C_2$ electrode delivered high specific capacitance, excellent power density, remarkable cyclic stability, and mechanical durability over 10,000 bending cycles. The assembled device successfully powered small electronics (LEDs and digital thermometers). Also, integrated with a pressure sensor to monitor human heartbeat signals in real time, with wireless data transmission to a mobile device. This work demonstrates the efficiency and applicability of $Fe_2O_3@Ti_3C_2$ flexible supercapacitors for next-generation wearable and biomedical electronics.

Over the past few decades, the drive to develop highly efficient, affordable, and environmentally friendly energy storage materials has grown significantly. This effort continues to evolve due to the impactful applications of these materials in flexible and wearable electronic devices[1–3]. Recently, weightless, portable, and flexible energy storage devices have become the prime necessities for developing stretchable electronics. Supercapacitors are the finest alternative as they can offer an incredibly higher power density than batteries/fuel cells. Flexible supercapacitors and batteries are still acclimated to power the wearable sensors and other prototypes[4–6]. Most electronic devices are powered by lithium/sodium-ion batteries. Still, these are harmful to the environment and hazardous to health due to organic solvents in their edifice[7,8]. On the other hand, flexible supercapacitors (FSCs) have prodigious mechanical compliance, high capacitance, excellent cyclic stability, and a quick charge–discharge rate with good power density. Also, FSCs work extraordinarily well under bending, shrinking, and twisting states, allowing them to extend to secondary devices (power backups) for next-generation flexible electronics[9]

According to the charge storage mechanism, supercapacitors (SCs) could be classified as electric double-layer capacitors (EDLCs), pseudocapacitors, or hybrid supercapacitors. Carbon-based materials (carbon nanotubes, carbon fiber, porous activated carbon, and graphene) are considered EDLCs-based electrode materials, whereas conducting polymers, transition metal oxides (TMOs), sulfides, and phosphides are considered electrodes with pseudocapacitive nature due to their redox processes[10,11]. Due to their fascinating physical and electrochemical properties, two-dimensional (2D) materials like metal chalcogenides, boron nitride, graphene, and MXenes have recently engrossed scientific researchers. The $M_{n+1}X_n$ structure of MXenes contains layers intercalated with an A element (like Al) in the MAX phase. The stacking arrangement of MXene layers is beneficial for easy ion insertion and exertion at the electrode–electrolyte interface[12,13]. Ti_3C_2 is a typical 2D MXene extensively studied for supercapacitors and batteries because of its excellent electrical conductivity, variable interlayer spacing, good hydrophilic surfaces, and great chemical stability. Despite its improved rate and outstanding cycle performance, the low specific capacitance restricts

---

[1]Future Energy and Innovation Laboratory, Central European Institute of Technology, Brno University of Technology, Brno, Czech Republic. [2]Faculty of Electrical Engineering and Computer Science, VSB - Technical University of Ostrava, Ostrava, Czech Republic. [3]Department of Chemical and Biomolecular Engineering, Yonsei University, Seoul, South Korea. [4]Department of Medical Research, China Medical University Hospital, China, Medical University, Taichung, Taiwan.
e-mail: Martin.Pumera@ceitec.vutbr.cz

the uses of Ti_3C_2 MXene[14–17]. Van der Waals interactions over prolonged cycles are the primary cause of anisotropy and restacking of MXene nanosheets[18]. These interactions limit the accessibility of ions to the interlayer sites, preventing full surface area utilization for electrochemical charge storage[19]. Hence, it is necessary to amplify Ti_3C_2 performance, such as specific capacitance, electrochemical stability, and tuneable mechanical robustness, by integrating with carbon-based materials, conductive polymers, metal oxides, phosphides, sulfides, and selenides, which serve as interlayer spacers. This synergistic combination could lead to improved electrochemical performance and increase Ti_3C_2 usefulness in a range of applications. TMOs, such as RuO_2, Fe_2O_3, NiO, ZnO, CuO, WO_3, TiO_2, SnO_2, and MnO_2, have been proven to provide better electrochemical stability than polymeric materials and a greater specific capacitance for supercapacitors compared to traditional carbon materials[19,20]. TMOs store energy through ion intercalation/deintercalation (redox pseudocapacitance) and provide quick diffusion paths and extra active sites. TMOs are one of the most regularly researched compounds due to their inexpensive cost and range of benefits[21–25]. However, TMOs exhibit ionic diffusivity, lower electronic conductivity, very short cycle life, and high resistance at the electrode–electrolyte interface. Therefore, incorporating conductive 2D material into the TMO matrix effectively solves these issues. Additionally, by acting as spacers, the TMO keeps the active surface area constant by preventing the MXene nanosheets from restacking.

Herein, we prepared a flexible supercapacitor using four different metal oxides (Fe_2O_3, MnO_2, NiO, and ZnO) combined with 2D Ti_3C_2 MXene. Although various metal oxides are employed to create composites with MXene, Fe_2O_3 composite with Ti_3C_2 exhibits improved qualities over other metal oxides because of its high stability, high conductivity, many valence states, strong catalytic activity, and low toxicity. Fe_2O_3 nanoparticles were evenly distributed over the sheets of Ti_3C_2 MXene in $Fe_2O_3@Ti_3C_2$ composite, improving the active site. The ferric oxide and titanium carbide ($Fe_2O_3@Ti_3C_2$) flexible asymmetric supercapacitor (FTASC) exhibits high specific capacitance (C_{sp}), power density, long-term cycling, and bending durability. The FTASC was coupled in series to power a digital thermometer and a red/blue light-emitting diode to provide a constant power source in different warps to demonstrate a practical portable application. Moreover, to demonstrate its applicability, the FTASC was connected to a pressure sensor to monitor a heartbeat in real time. The heartbeat signal was monitored on a smartphone *via* wireless communication (Fig. 1). This work presents the first demonstration of a highly flexible, $Fe_2O_3@Ti_3C_2$-based asymmetric supercapacitor (FTASC) that not only delivers superior energy storage performance but also integrated into a real-time, wireless health monitoring system, showcasing its strong potential for next-generation wearable biomedical devices.

Results

Structural and morphological analysis of prepared composites

A flexible and robust device was fabricated using a $Fe_2O_3@Ti_3C_2||Ti_3C_2$ asymmetric supercapacitor (FTASC). To illustrate a real time health monitoring application, the FTASC powered a pressure sensor to track a human heartbeat in real time *via* wireless communication using a cellular device. Before measuring the electrochemical performance, it is necessary to examine the morphological and chemical structure of the $Fe_2O_3@Ti_3C_2$ hybrid nanocomposite. A comprehensive synthesis process of the $Fe_2O_3@Ti_3C_2$ and other nanocomposite preparation are provided in methodology section. Figure 2A displays the XRD patterns of Ti_3C_2 and $Fe_2O_3@Ti_3C_2$. The exfoliated Ti_3C_2 XRD exhibits some intense and broad characteristic peaks at 9°, 18.7°, 34.6°, 36°, 39°, 42°, 46°, and 60.5°, which are indexed as the (002), (004), (101), (102), (103), (105), (106), and (110) hkl plane, respectively[26]. The peaks related to the (101) and (105) planes are associated with TiC. In the case of $Fe_2O_3@Ti_3C_2$, new peaks of Fe_2O_3 were observed along with the Ti_3C_2 peaks at 2θ range of 25.2°, 33.12°, 36.63°, 41.64°, 49.47°, 55.08°, 57.42° and 64° as ascribed to the (012), (101), (014), (110), (113), (024), (116), and (300) hkl plane, respectively[27]. This diffraction Braggs angle indicates the crystalline structure of Fe_2O_3 nanoparticles, which was matched with JCPDS card number 01-089-0598 for its rhombohedral crystal system matrix[28]. The Supplementary Fig. 1 also contains XRD patterns of various MXene composites ($MnO_2@Ti_3C_2$, $NiO@Ti_3C_2$, and $ZnO@Ti_3C_2$). The XRD peaks of $Fe_2O_3@Ti_3C_2$ and the non-appearance of other peaks confirm the successful amalgamation of Ti_3C_2 with Fe_2O_3 and ratify phase purity.

For pristine Ti_3C_2, the (002) peak appears at 9°, whereas in $MnO_2@Ti_3C_2$, $Fe_2O_3@Ti_3C_2$, $NiO@Ti_3C_2$, and $ZnO@Ti_3C_2$, slight shifts are observed at 8.6°, 5°, 8.7°, and 8.8° respectively resulting in an expansion of the d-spacing (using Bragg's Law) from 9.8 to 17.6 A° are discussed in Supplementary Table 1. When four distinct metal oxides are added to the Ti_3C_2, a weak peak of MXene (002) moves from 9° to 5° to the left. This indicates that Fe_2O_3 functions as an effective interlayer spacer, enhancing the interlayer distance between Ti_3C_2 layers by preventing restacking[29]. This increased interlayer distance can enhance the use of active sites and is advantageous for recurrent ion intercalation/diffusion kinetics. The XRD results confirm the successful synthesis of the $Fe_2O_3@Ti_3C_2$ composite with a morphology that makes it easier for the ions in the electrolyte to move freely throughout the electrochemical process. Figure 2B displays the Raman spectra of delaminated Ti_3C_2 and $Fe_2O_3@Ti_3C_2$. The vibrational modes of Ti_3C_2 were noticed at 162 cm^{-1}, 258 cm^{-1}, and 604 cm^{-1}. These vibrational modes correlate to Ti-C and Ti-O bonds[30]. In the case of $Fe_2O_3@Ti_3C_2$, along with Ti_3C_2 peaks, some new peaks of Fe_2O_3 were observed at A_{1g} modes of 228 cm^{-1} and 499 cm^{-1}, and E_{2g} modes of 289 cm^{-1}, 409 cm^{-1}, and 609 cm^{-1}. The Fe-O mode stretching between Fe and O atoms is linked to the peaks at 289 cm^{-1} and 409 cm^{-1}. The presence of highly crystalline hematite and the interaction of two magnons generated on antiparallel near-spin sites results in the forming some less strong peaks in the 1000–1500 cm^{-1} region[31]. Figure 2C–F displays SEM and EDS images of $Fe_2O_3@Ti_3C_2$ nanocomposite. Figure 2C shows the distinct spaces between the delaminated Ti_3C_2 MXene nanosheets. This might improve the contact between the electrode and electrolyte, leading to effective ionic transport and pseudo-capacitance performance. The synthesized Fe_2O_3 nanoparticles (Fig. 2D), exhibit a spherical shape with clusters of aggregated nanoparticles.

Fig. 1 | Real-time health monitoring applications by integrated $Fe_2O_3@Ti_3C_2||Ti_3C_2$-based flexible device. A Schematic illustration of the $Fe_2O_3@Ti_3C_2||Ti_3C_2$ ASC fabrication. **B** Integrated pressure sensor with two series-connected FTASCs for real time radial pulse monitoring.

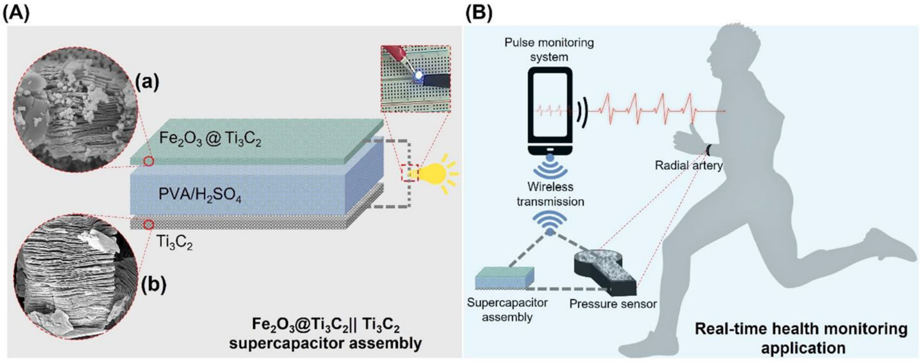

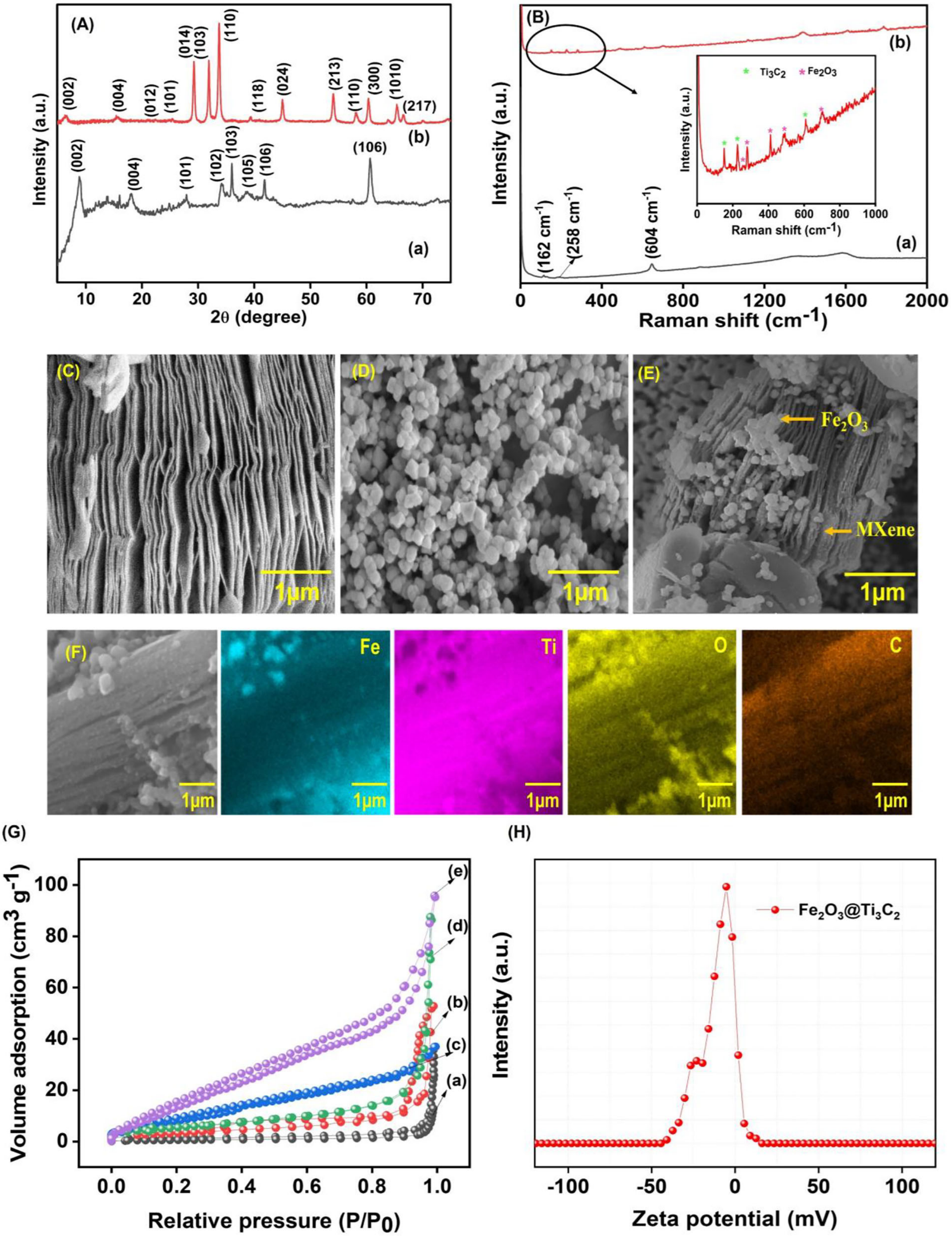

Fig. 2 | Structural and morphological characterization. **A** XRD spectra of (a) Ti_3C_2 MXene; (b) $Fe_2O_3@Ti_3C_2$. **B** Raman spectra of (a) Ti_3C_2 MXene; (b) $Fe_2O_3@Ti_3C_2$. SEM images of **C** delaminated Ti_3C_2 MXene; **D** Fe_2O_3; **E** $Fe_2O_3@Ti_3C_2$. **F** Elemental mapping from SEM image of $Fe_2O_3@Ti_3C_2$ nanocomposite. **G** Surface area analysis of (a) Ti_3C_2; (b) $ZnO@Ti_3C_2$; (c) $NiO@Ti_3C_2$; (d) $MnO_2@Ti_3C_2$; (e) $Fe_2O_3@Ti_3C_2$ and **H** Zeta potential of $Fe_2O_3@Ti_3C_2$.

Figure 2E shows the Fe_2O_3 nanoparticles anchored on the surface of the layers of Ti_3C_2. The Supplementary Information (Supplementary Fig. 2) also contains SEM images of pristine and various MXene composites ($MnO_2@Ti_3C_2$, $NiO@Ti_3C_2$, and $ZnO@Ti_3C_2$). The SEM image of MnO_2 NPs exhibits a flower-like structure. The synthesized NiO nanoparticles exhibit a spherical shape nanoparticle and the prepared ZnO shows aggregation of petals and forms flower like morphology (Supplementary Fig. 2). Compared to the MnO_2, NiO, and ZnO, the Fe_2O_3 combined with

Ti_3C_2 have two functions: i) they operate as interlayer spacers to increase the Ti_3C_2 MXene interlayer distance, and ii) they act as an additional electrocatalytic active site for the reaction. Figure 2F displays the elemental mapping of titanium (Ti), iron (Fe), carbon (C), and oxygen (O) elements in the prepared nanocomposite. It indicates that the synthesized nanocomposite is devoid of contaminants without other components. Figure 2G exhibits the BET surface area of 18, 29, 53, 85, and 112 $m^2\ g^{-1}$ for Ti_3C_2, ZnO@Ti_3C_2, NiO@Ti_3C_2, MnO_2@Ti_3C_2, and Fe_2O_3@Ti_3C_2 composite, respectively. The open loop in the Fe_2O_3@Ti_3C_2 isotherm confirms the existence of micro and mesopores. The delaminated layers of Ti_3C_2, together with the aggregation of Fe_2O_3 particles, increase the specific surface area and pore volume. The blend of micro and mesopores also recommends effective ion transfer, enhancing electrochemical behavior. The nanocomposite's pore size and pore volume are discussed in Supplementary Table 2. Zeta potential was employed to determine the charge at the surface, as shown in Fig. 2H. An increased negative or positive zeta potential indicates the stability of nanosuspension caused by electrostatic repulsive forces between nanoparticles. The lowest zeta potential value causes nanoparticle agglomeration because of repulsive interactions, mainly van der Waals forces. The zeta potentials of the synthesized Ti_3C_2 and Fe_2O_3@Ti_3C_2 were −16.8 mV and −0.27 mV, respectively, suggesting that it is much more agglomerated and that the intercalation of Ti_3C_2 nanosheets and Fe_2O_3 nanoparticles was generated by van der Waals force. The zeta potential of Ti_3C_2 (−16.8 mV), MnO_2@Ti_3C_2 (−1.3 mV), NiO@Ti_3C_2 (−3.2 mV), and ZnO@Ti_3C_2 (−9.5 mV) are shown in Supplementary Fig. 3. In comparison to the other nanocomposites, this result shows that the Fe_2O_3 can be efficiently bonded to the Ti_3C_2 surface, changing the charge densities because of the high surface activity of the Fe_2O_3 with the widespread cationic groups.

The distinctive spectrum of the Ti 2p, Fe 2p, C 1s, and O 1s elements alone was noticed in the survey spectrum of Fe_2O_3@Ti_3C_2 (Supplementary Fig. 4a))[32]. From Supplementary Fig. 4b, the deconvolution of C 1s is convoluted into three peaks, positioned at 280, 282, and 284 eV, representing Ti-C, C-Ti-O, and C-C, respectively. The O 1s spectrum in Supplementary Fig. 4c) shows two peaks, attributed to Ti-O (526 eV) and C-Ti-O_x (527 eV). The peak at 529.5 eV corresponds to the Fe-O bond, indicating a preferred interaction between Ti_3C_2 and Fe^{3+} ions. Ti 2p deconvoluted into four prominent peaks (Supplementary Fig. 4d). The main peak at 454 eV (Ti-C) and the other convoluted peaks are noticed at 452 eV, 456 eV, and 460 eV, corresponding to Ti^{3+}, Ti^{4+}, and Ti-O, respectively. Supplementary Fig. 4e shows two primary peaks centered at 710 eV for Fe^{2+} and 722 eV for Fe^{3+} of Fe, indicating a successful combination of Ti_3C_2 with Fe_2O_3. Additionally, there is a shakeup satellite peak, termed Fe^{3+} of the hematite phase Fe_2O_3. These findings demonstrate strong interactions between the two pristine components, resulting in a compact heterojunction composite.

Electrochemical performance of three electrode cell configuration

Using a conventional three-electrode cell configuration in 1 M H_2SO_4, the electrochemical performance of the constructed half-cells, Ti_3C_2, Fe_2O_3@Ti_3C_2, MnO_2@Ti_3C_2, NiO@Ti_3C_2, and ZnO@Ti_3C_2, was evaluated (Fig. 3A). Due to the presence of oxygen functional groups, the fabricated electrodes display rectangular charge and discharging curves with redox behavior. A higher integral area in the CV curve of the Fe_2O_3@Ti_3C_2 electrode indicates faster reaction kinetics and an improved specific surface area when compared to the Ti_3C_2, MnO_2@Ti_3C_2, NiO@Ti_3C_2, and ZnO@Ti_3C_2 electrodes. This enhancement is due to Ti_3C_2 and Fe_2O_3 having strong interfacial contact, which promotes effective interaction with the electrolyte, greater specific surface areas, and efficient electron transport. The GCD curves were examined at current density (0.5 A g^{-1}) for the Ti_3C_2, Fe_2O_3@Ti_3C_2, MnO_2@Ti_3C_2, NiO@Ti_3C_2, and ZnO@Ti_3C_2 electrodes, respectively (Fig. 3B). Each of the GCD curves displays a quasi-triangle shape with varying charge–discharge times, demonstrating the composite's good reversibility and capacitive behavior. Figure 3C displays the specific capacitance contribution of each of the constructed electrodes. The as-fabricated Fe_2O_3@Ti_3C_2 electrode had the highest specific capacitance of 213 Fg^{-1}, surpassing that of Ti_3C_2 (66 Fg^{-1}), MnO_2@Ti_3C_2 (133 Fg^{-1}), NiO@Ti_3C_2 (99 Fg^{-1}), and ZnO@Ti_3C_2 (78 Fg^{-1}) due to the inferior performance of MnO_2@Ti_3C_2, NiO@Ti_3C_2, and ZnO@Ti_3C_2 is lesser than Fe_2O_3@Ti_3C_2, resulting in an insufficient number of active sites. Moreover, there is minimal intercalation of MnO_2, NiO, and ZnO into the layers of Ti_3C_2, which fails to effectively hinder its restacking tendency. Fe_2O_3 further opens up the active sites and allows optimal charge carrier flow by decreasing the accumulation of layers between MXene layers, which improves the electrochemical reaction. Figure 3D displays each electrode's Nyquist curves. A solution resistance is indicated by the R_S values of the fabricated electrodes (Ti_3C_2, MnO_2@Ti_3C_2, NiO@Ti_3C_2, ZnO@Ti_3C_2, and Fe_2O_3@Ti_3C_2). The electrodes' charge-transfer resistance (R_{CT}) is determined to be 41.9 Ω, 14.8 Ω, 17.9 Ω, 25.4 Ω, and 7 Ω. The straight line in the low-frequency range displays the electrode material's ideal capacitance behavior. Because of the capacitance contribution and the conductivity gain of metal ions, Fe_2O_3@TiC_2 had the lowest R_{CT} value, indicating low internal resistance, good conductivity, and the best charge transfer capabilities. The CV curves' scan rates for the Fe_2O_3@Ti_3C_2 electrodes with a potential window of −0.2 to 0.8 V are shown in Fig. 3E. The as-fabricated Fe_2O_3@Ti_3C_2 electrode displays a distinct and less intense oxidation peak at 0.5 V and a reduction peak at 0.2 V. It elucidates a pair of cathodic and anodic peaks due to the reversible reactions of iron's oxidation states ($Fe^{2+}\leftrightarrow Fe^{3+}$). These redox peaks indicate typical faradaic charge storage owing to the presence of Fe_2O_3 in Ti_3C_2. The CV curves show good stability even from low to high scan rates and retain the redox peaks, indicating stable and fast electrochemical charge storage.

The flexible Fe_2O_3@Ti_3C_2 electrode's rate performance in 1 M H_2SO_4 electrolyte at different current densities were assessed through the analysis of GCD data (Fig. 3F). The quasi-triangular shape with the trivial IR drops of the curve exhibits the combination of pseudocapacitive behavior and excellent reversibility, which was well agreed with the performance observed from CV curves. The lack of substantial faradaic processes is indicated by the linear stability of the potential throughout time at high current density, indicating excellent rate performance and a quick ion transport mechanism. The specific capacitance (C_{sp}) of Fe_2O_3@Ti_3C_2 is linearly lowered at varying current densities (Fig. 3G). Additionally, it is observed that the discharge time decreases with increasing current density. Rapid ion transport at the electrode–electrolyte interface and inadequate use of the effective surface area are the causes of this phenomenon. The CV and GCD curves of MnO_2@Ti_3C_2, NiO@Ti_3C_2, and ZnO@Ti_3C_2 electrodes are shown in Supplementary Fig. 5. There are multiple contributing factors to the Fe_2O_3@Ti_3C_2 electrode's remarkable specific capacitance. First, Ti_3C_2 surface terminations form strong functional bonds with Fe_2O_3, which has a synergistic impact that improves energy storage capacity. Second, the Fe_2O_3@Ti_3C_2 electrode's crumpled MXene sheets increase surface area while maintaining the material's inherent qualities, which is kinetically advantageous throughout the charge and discharge operations. Thirdly, by serving as interlayer spacers and enhancing the exposure of electrochemically active areas, Fe_2O_3@Ti_3C_2 inhibit the aggregation of MXene sheets while promoting quick mass transfer. These synergistic effects result from the Fe_2O_3@Ti_3C_2 electrode's improved electrochemical performance and greater ion transfer capability. Raman analysis during charging and discharging further confirms its pseudocapacitance and the synergistic nature of Fe_2O_3@Ti_3C_2 (Supplementary Fig. 6). Characteristic Fe-O stretching modes (228, 289, and 409 cm^{-1}) exhibits intensity shifts in the peaks, indicating the Fe^{3+}/Fe^{2+} redox transition responsible for pseudocapacitive charge storage. In the case of discharging, the increased intensity peaks return to its original position which shows reversible redox which is a key feature of pseudocapacitance. Simultaneously, stable Ti_3C_2 vibrational bands confirmed its structural integrity and role as a conductive framework. These results support the synergistic interaction between Fe_2O_3 and Ti_3C_2. Figure 3H the bar diagram shows the diffusion-controlled and capacitive contributions of the fabricated Fe_2O_3@Ti_3C_2 electrode at different scan rates (10, 30, 50, 70, and, 90 mV/s). The corresponding capacitive contributions are 42%, 58%, 66%, 79%, and 83%, respectively. Figure 3I shows the

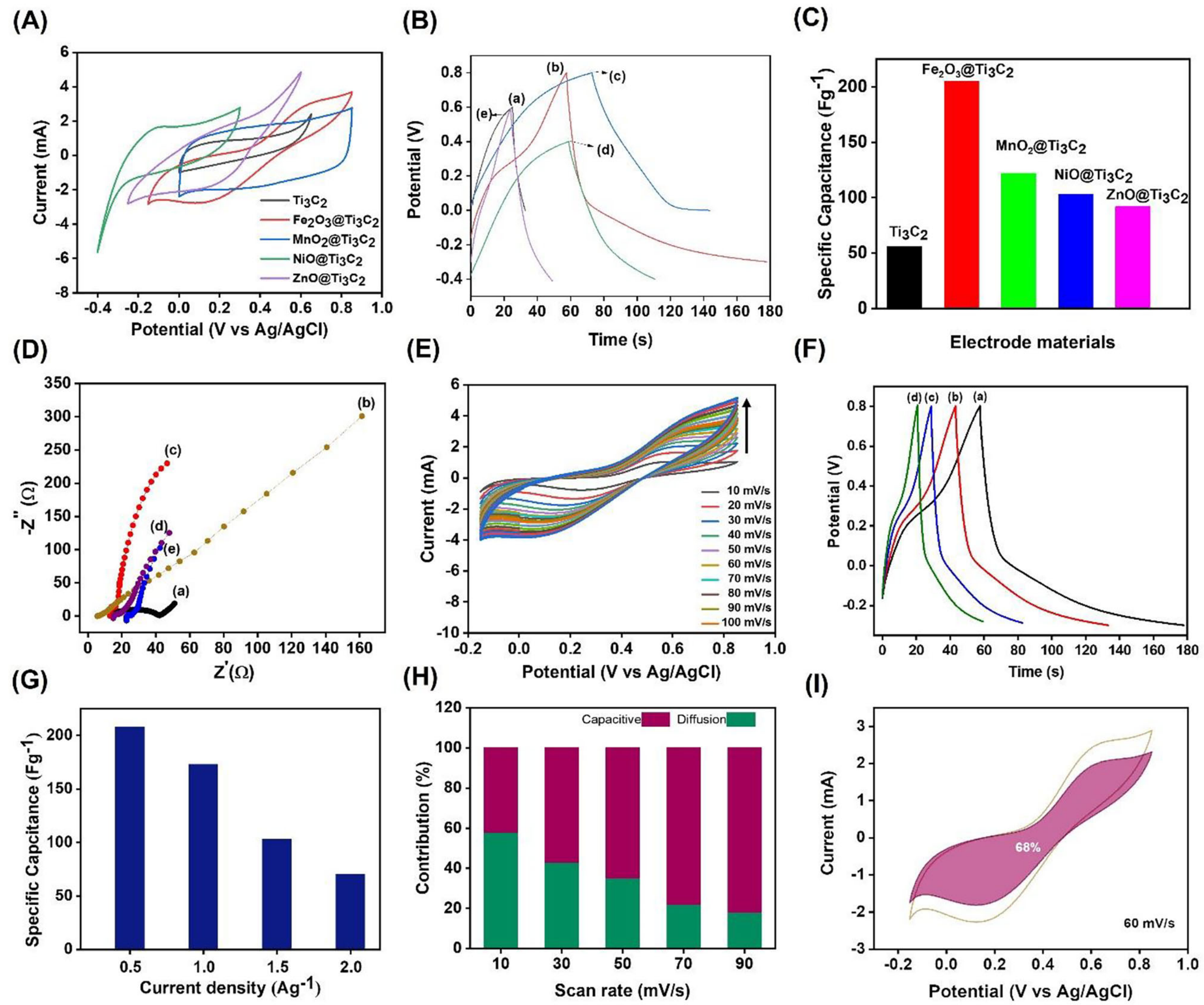

Fig. 3 | Electrochemical performances of flexible electrodes. **A** Comparison of cyclic voltammograms (10 mV s^{-1}). **B** Galvanostatic charge–discharge curves of (a) Ti_3C_2; (b) $Fe_2O_3@Ti_3C_2$; (c) $MnO_2@Ti_3C_2$; (d) $NiO@Ti_3C_2$; (e) $ZnO@Ti_3C_2$ in 1 M H_2SO_4 electrolyte. **C** Comparison bar graph of fabricated electrodes *versus* specific capacitance. **D** Nyquist plot of (a) Ti_3C_2; (b) $Fe_2O_3@Ti_3C_2$; (c) $MnO_2@Ti_3C_2$; (d) $NiO@Ti_3C_2$; (e) $ZnO@Ti_3C_2$. **E** Cyclic voltammograms of $Fe_2O_3@Ti_3C_2$ at various scan rates. **F** Galvanostatic charge–discharge curves of $Fe_2O_3@Ti_3C_2$ at different current densities: (a) 0.5 Ag^{-1}; (b) 1 Ag^{-1}; (c) 1.5 Ag^{-1}; (d) 2 Ag^{-1}. **G** Graph of specific capacitance *versus* current density. **H**, **I** Capacitive and diffusion-controlled contribution calculated at different scan rates of $Fe_2O_3@Ti_3C_2$ electrode.

qualitative comparison of the diffusion-controlled and total capacitance of the $Fe_2O_3@Ti_3C_2$ electrode for a scan rate of 60 mV/s. The diffusion-controlled mechanism is discovered to dominate the electrode's capacitance at low scan rates. The intercalation/deintercalation contribution decreases as the scan rate increases, while the non-diffusion controlled capacitive begins to increase [33].

Fabrication of flexible asymmetric supercapacitor (ASC) device

A flexible asymmetric supercapacitor (ASC) device was constructed with PVA/H_2SO_4 gel electrolyte. The flexible $Fe_2O_3@Ti_3C_2||Ti_3C_2$ (FTASC) schematic is shown in Fig. 4A. Figure 4B, C illustrate CV curves over different scan rates and the GCD with different current densities for the fabricated flexible device. The CV curves are symmetric at all scan rates and provide a clear picture of the optimal capacitive behavior of FTASC. The maximum specific capacitance of 123 F g^{-1} at the current density of 0.5 Ag^{-1}, is marginally lower than the value observed in the 1 M H_2SO_4 aqueous electrolyte because of the PVA/H_2SO_4 electrolyte's lower ionic coefficient and the inadequate transport of ions toward the interface between the electrolyte and the active material. The specific capacitance of the fabricated device at different current densities is provided in Fig. 4D, where it decreases linearly. Figure 4E shows the cyclic voltammetry data of the diffusion-controlled and total capacitance of the $Fe_2O_3@Ti_3C_2||Ti_3C_2$ electrode at a scan rate of 50 mV/s. The contribution at different scan rates for $Fe_2O_3@Ti_3C_2||Ti_3C_2$ was shown in Fig. 4F. The capacitive contribution gradually increases from 45%, 56, 69%, 75%, and 80% under a scan rate of 10, 30, 50,70, and 90 mV/s. The plot indicates that when the scan rate increases, the capacitive contribution increases as well. With lowering scan rates, the diffusion-controlled contribution is shown to rise. This could be explained by the longer time available for the H^+ ion diffusion into the electrodes at lower scan rates. Diffusion kinematics dominates the electrochemical performance of the two-electrode system at low scan rates. A constant current density of 2 Ag^{-1} was used to evaluate the cycling stability of the flexible FTASC across 10,000 cycles (Fig. 4G). As shown in Fig. 4G, the specific capacitance of the FTASC increased progressively during the initial 100 cycles. This phenomenon is commonly attributed to an electrochemical activation process, where repeated ion intercalation/deintercalation improves electrode–electrolyte interface contact, enhances electrolyte penetration, and gradually exposes more electrochemically active sites. Additionally, this may involve minor structural rearrangements or improved conductivity due to better alignment of conductive pathways. Once stabilized, the capacitance plateau indicates that the

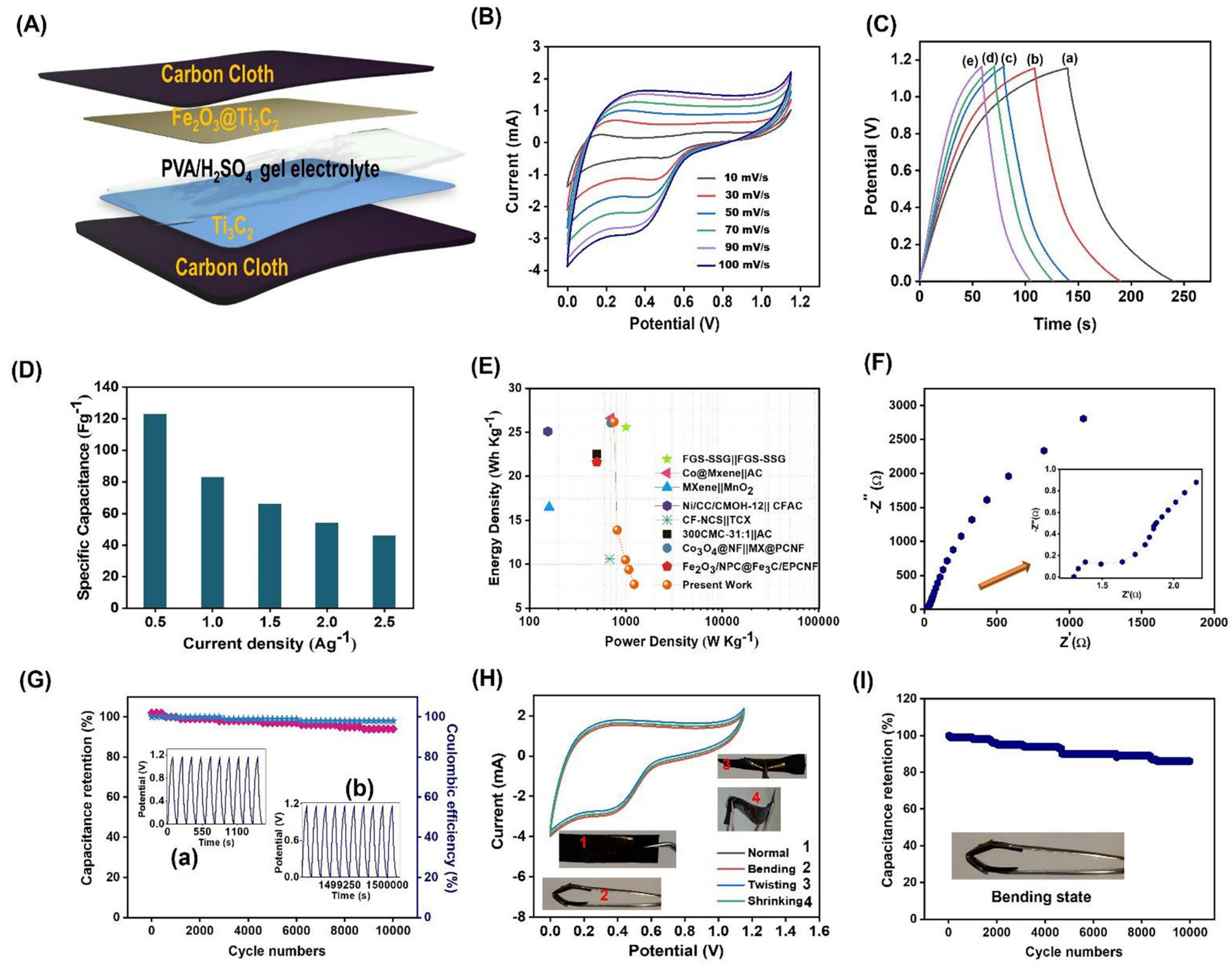

Fig. 4 | Electrochemical performance of $Fe_2O_3@Ti_3C_2||Ti_3C_2$ in PVA/H_2SO_4 gel electrolyte. **A** Schematic illustration of the cell assembly. **B** Cyclic voltammograms at various scan rates. **C** Galvanostatic charge–discharge curves at different current densities: (a) 0.5 Ag^{-1}; (b) 1 Ag^{-1}; (c) 1.5 Ag^{-1}; (d) 2 Ag^{-1}; (e) 2.5 Ag^{-1}. **D** Specific capacitance *versus* different current densities. **E**, **F** Capacitive and diffusion-controlled contributions are calculated at different scan rates. **G** Cyclic stability and coulombic efficiency (%) (insert (a) first and (b) last 10 cycles). **H** FTASC device's cyclic voltammograms were -recorded at different positions angles. **I** Cyclic stability at a bending state over 10,000 cycles.

electrode reached an optimal state for charge storage[34]. The maximum values observed are 96% coulombic efficiency and 94% capacitance retention. Examining the fabricated ASC mechanical characteristics, output power, and adaptability is essential to validate its suitability as a portable power source for healthcare applications. Hence, device flexibility was investigated by CV analysis under normal, bending, twisting, and shrinking conditions (Fig. 4H). The long-term mechanical and electrochemical stability of the FTASC under repeated bending conditions (Fig. 4I) confirms its suitability for integration with flexible sensing devices. After 10,000 mechanical cycles, the FTASC retained 85% of its initial capacitance, demonstrating strong mechanical rigidity and resilience.

This stability ensures consistent power output, when integrated with a pressure sensor for real-time pulse monitoring. The device maintained stable performance throughout extended operation. This indicates that the FTASC not only preserves its energy storage capabilities under continuous mechanical stress but also supports the stable operation of the sensor–supercapacitor system. The slight decrease in capacitance may stem from structural changes in the $Fe_2O_3@Ti_3C_2$ electrode or the polymer electrolyte's deformation during ion intercalation/deintercalation processes, which are typical in pseudocapacitive systems[35]. Furthermore, SEM and XRD studies were performed to evaluate the morphological and structural evolution of the $Fe_2O_3@Ti_3C_2$ composite before and after electrochemical analysis. Despite 10,000 consecutive cycles, the results (Supplementary Fig. 7) reveal no significant morphological alterations. Even after 10,000 cycles, the $Fe_2O_3@Ti_3C_2$ electrode is stable and does not form secondary phases. However, the (002) peak shifts to 5° from 10.2°, resulting in a decrease in the d-spacing from 15.9 to 10.5 A°. The shifts to a higher angle after 10,000 cycles indicate that repeated cycling induces mechanical stress on the Ti_3C_2 layers, forcing them to pack closer together. This can result in a permanent reduction of the interlayer distance.

A Ragone plot shows the power (P) and energy (E) densities of the FTASC and reveals the highest energy density of 26.15 Wh kg^{-1} at 0.5 Ag^{-1} and a power density of 1260 W kg^{-1} at 2.5 Ag^{-1}, respectively. A Ragone plot comparing the performance of $Fe_2O_3@Ti_3C_2||Ti_3C_2$ with different reported supercapacitors is shown in Fig. 5A. Upon comparing the obtained energy and power densities of the ASC devices with previous research on metal oxide and MXene supercapacitor electrodes (Supplementary Table 3), it was found that the majority of the constructed supercapacitors were capable of producing either high or low energy densities. The assembled FTASC observes notable energy density and power density. Measurements of impedance were done between 100 kHz and 1 Hz. Typical capacitor behavior is shown by the linear vertical line in the low-frequency zone parallel to the imaginary component of the impedance. The faradaic resistance behavior, which is

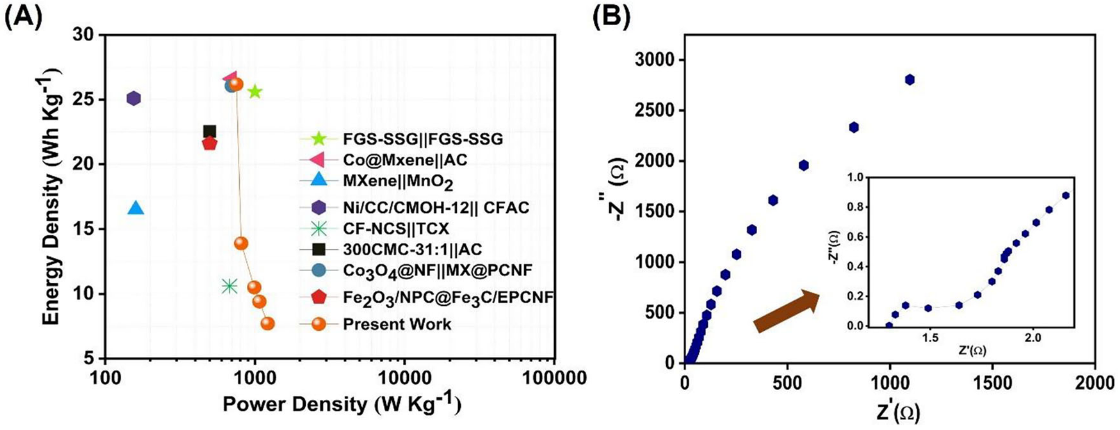

Fig. 5 | Electrochemical performance of $Fe_2O_3@Ti_3C_2||Ti_3C_2$ in PVA/H_2SO_4 gel electrolyte. **A** Comparison of power and energy densities of cutting-edge supercapacitor (SC) devices using the Ragone plot. **B** Nyquist plot (inset displays enlarged image).

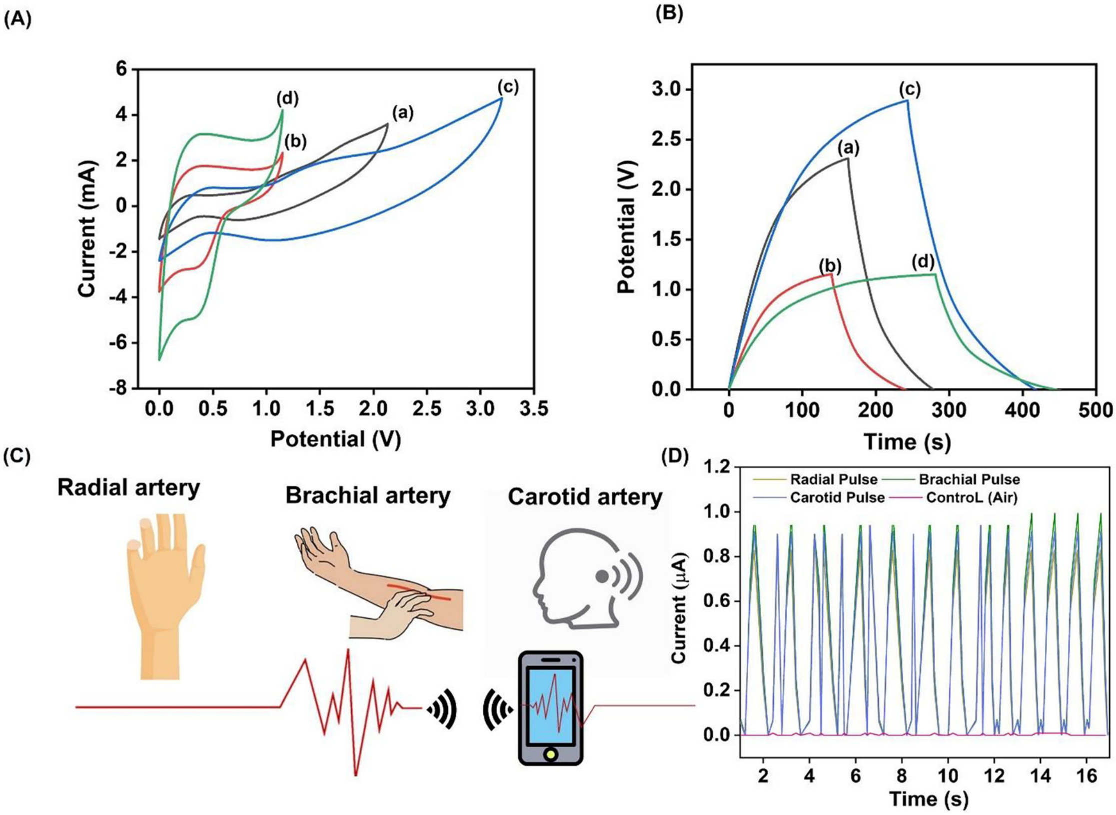

Fig. 6 | Flexible interdigitated $Fe_2O_3@Ti_3C_2||Ti_3C_2$ FTASC for powering health monitoring systems. **A** and **B** show cyclic voltammograms and galvanostatic charge–discharge curves of $Fe_2O_3@Ti_3C_2||Ti_3C_2$ in both (a, c) series and (b, d) parallel configurations. **C** Schematic illustration of real time wireless (a) radial, (b) brachial, and (c) carotid pulse monitoring. **D** The recorded live (a) radial, (b) brachial, and (c) carotid pulse signals *via* the cellular device.

linked to the ion movement between the electrode and electrolyte and limits the diffusion rate, is correlated with the semicircle diameters (Fig. 5B). The circuit consists of charge transfer resistance R_{ct} (1.63 Ω cm^2) and intrinsic resistance R_s (1.29 Ω cm^2).

Real time application of flexible interdigitated $Fe_2O_3@Ti_3C_2||Ti_3C_2$ FTASC for powering health monitoring systems

The practical applications of the fabricated FTASC when connected in series or parallel were tested using CV and GCD analysis (Fig. 6A, B). In addition, two and three serially and parallelly connected FTASCs had two (2.2 V) and three times (3.3 V) the increase in output voltage as compared to a single FTASC with an operating potential window of 1.1 V (Fig. 4B) and a similar discharge time was observed from GCD analysis (Fig. 4C). The fabricated flexible asymmetric supercapacitor encased with glass slides was connected to power-up LEDs (blue and red) for more than 1 min (Supplementary Fig. 8a and Supplementary Videos 1–3). Furthermore, the device operated a digital thermometer display (Supplementary Fig. 8b). The FTASC was used to power a pressure sensor to construct a real time wearable application. Figure 6C shows the schematic illustration of real time wireless radial, brachial, and carotid pulse monitoring. The FTASC was charged using an electrochemical workstation and variations in current output in response to pressure applied to the active surface were identified by the integrated pressure sensor. The integrated device was applied to the subject's skin (radial, brachial, and carotid) to measure artery pulse, the software captured periodic current signals that showed a heart rate of about ≈72 beats per minute (Fig. 6D). The pressure sensor of the serially connected FTASC was constantly powered for 500 s at a rate of approximately 13 μW following a 2.2 V charge. Lastly, a smartphone was used to wirelessly transmit data in real time to monitor the pulse tracker data produced by the pressure sensor. These results demonstrated that the portable integrated device can wirelessly monitor individual health parameters in real time with improved stability and can discretely accumulate signals. According to the aforementioned experimental findings, FTASC is a viable option for powering portable electronic and medical devices.

Discussion

In this study, we successfully fabricated a flexible binder-free supercapacitor based on $Fe_2O_3@Ti_3C_2$ nanocomposite. The fabricated $Fe_2O_3@Ti_3C_2$ half-cell showed a maximum specific capacitance of 213 Fg^{-1} in 1 M H_2SO_4 aqueous solution. The $Fe_2O_3@Ti_3C_2||Ti_3C_2$ ASC operates in a wide potential window from 0 to 1.1 V and exhibits high specific capacitance (123 Fg^{-1}) with a maximum energy density of 26.15 Wh kg^{-1} at 880 W kg^{-1}. The FTASC maintains 94% of its initial specific capacitance and 96% coulombic efficiency after 10,000 cycles and also exhibits 85% mechanical stability in a bent state across 10,000 cycles. Compared to the other metal and MXene nanocomposites, these values are substantially higher. Furthermore, the fabricated FTASCs are connected in parallel and series to improve the output current/potential as demonstrated in our study powering LEDs and digital thermometers. For portable electronics, the fabricated device could surpass the energy density gap between supercapacitors and batteries. Second, in the proof of concept tests for real-time application, the fabricated FTASC was connected to a portable biomonitoring system (pressure sensor), and live artery pulse signals (72 bpm) were detected. The findings underscore the potential of $Fe_2O_3@Ti_3C_2$ as a sustainable, flexible, lightweight, and portable energy storage solution, developed through a versatile hybrid approach suitable for various electronic device applications. These promising results establish $Fe_2O_3@Ti_3C_2$ electrode as a high-performance, flexible, and sustainable electrode material for next-generation energy storage devices. However, there are significant hurdles to real-world implementation. In particular, the scalability of the synthesis and device fabrication processes must be optimized for mass production while maintaining consistent quality and cost efficiency. Furthermore, biocompatibility testing is critical for applications in wearable or implantable biomedical devices to assure long-term safety. Finally, future research should focus on connecting these supercapacitors to IoT platforms, allowing for real-time monitoring, data transmission, and intelligent energy management in smart electronic devices.

Methods

Materials

The $Ti_3C_2T_x$ MXene powders were purchased from Laizhou Kai Ceramic Materials Co. Ltd. (Hong Kong). Polyvinyl alcohol (PVA, Mw; 8000), sulfuric acid (H_2SO_4), ferric sulfate ($Fe(SO_4)_3$), ferric chloride ($FeCl_3$), potassium hydroxide (KOH), manganese(II) sulfate ($MgSO_4$), sodium hydroxide (NaOH), nickel sulfate hexahydrate ($NiSO_4{\cdot}6H_2O$), zinc acetate dihydrate ($Zn(CH_3CO_2)_2{\cdot}2H_2O$), ethanol, dimethyl sulfoxide (DMSO), polyvinylidene fluoride (PVDF), and n-methyl-pyrrolidone (NMP) were purchased from Sigma Aldrich. The carbon fabric was purchased from a U.S. fuel cell retailer. Interlink Electronics, Inc. supplied the pressure sensor. No additional purification or modification was applied to any of the components.

Delamination process of $Ti_3C_2T_x$ MXene

Delamination was successfully performed by sonication using DMSO as an intercalant to separate the layers of MXene, which is in favor of increasing the $Ti_3C_2T_x$ MXene interlayer gap. First, $Ti_3C_2T_x$ was dissolved in DMSO and left to stir overnight at room temperature. To separate the intercalated $Ti_3C_2T_x$ powder, the colloidal residue was centrifuged for 10 min at 3000 rpm. After that, it was cleaned with DI water and sonicated for five hours. Finally, the blackish powder was gathered and left to dry overnight at 70 °C [36].

Preparation of Fe_2O_3 nanoparticles

Appropriate $FeCl_3$ and $Fe(SO_4)_3$ concentrations were combined with 100 mL of DI water and magnetic stirring for an hour at 80 °C to create Fe_2O_3 nanoparticles. Next, as the precipitating agent, 50 mL of 2 M KOH aqueous solution was added drop-wise until pH 11 was attained. Then, the precipitates were gathered and centrifuged at 5000 rpm. Following many washes with distilled water/ethanol, the resulting blackish-brown powder was dried for 4 h at 400 °C [37].

Preparation of MnO_2 nanoparticles

MnO_2 nanoparticles were prepared via a co-precipitation technique using manganese acetate [$Mn(CH_3CO_2)_2$] and potassium permanganate ($KMnO_4$). A 0.004 mol of manganese acetate was dissolved into 100 ml of DI water followed by stirring for 60 min at room temperature. Then, 100 ml of 0.02 M potassium permanganate solution was added slowly into the stocked solution and stirred for 2 h. The final brown precipitate was filtered and washed with DI water and ethanol several times. The blackish-brown powder was dried at 100 °C for 24 h.

Preparation of NiO nanoparticles

The chemical co-precipitation method was used to synthesize NiO nanoparticles. Initially, 0.50 g NaOH and 0.7 g PVP were dissolved in 100 ml distilled water using a magnetic stirrer. Then 1.74 g Ni $(NO_3)_2{\cdot}6H_2O$ was dissolved in 60 ml of distilled water and added drop by drop continuously in the NaOH solution at room temperature. The final sample was centrifuged and washed with distilled water/ethanol 3–4 times and dried at 80 °C in the hot air oven.

Preparation of ZnO nanoparticles

A 2.5 g of Zinc chloride was mixed in 50 ml ethanol using a magnetic stirrer for 40 min. 1.6 g of Sodium hydroxide pellets were then dissolved in 10 ml of DI water and added dropwise into the Zinc chloride solution at room temperature. The final white powder was washed with DI water till the pH was 7. The powder was then dried at 120 °C for 24 h.

Preparation of $Fe_2O_3@Ti_3C_2$ nanocomposite

By adopting the simple ultrasonication approach, $Fe_2O_3@Ti_3C_2$ was created. 150 mg of Fe_2O_3 was added to an aqueous solution after 0.03 mol of Ti_3C_2 and 150 mL of DI water were combined under ultrasonication. Filtered and cleaned with DI water, a dark slurry of $Fe_2O_3@Ti_3C_2$ nanocomposite was obtained. The resultant product was dried at 80 °C in a hot air oven for 24 h. Finally, a black powder was labeled as FT.

Preparation of $MnO_2@Ti_3C_2$ nanocomposite

A $MnO_2@Ti_3C_2$ was prepared using the facile ultrasonication method where 0.03 mol of Ti_3C_2 was mixed with 150 mL of DD water under ultrasonication and 150 mg of MnO_2 was added in the Ti_3C_2 aqueous suspension. A black slurry of $MnO_2@Ti_3C_2$ nanocomposite was filtered and washed with DI water. The obtained product was dried in a hot air oven at 80 °C for 24 h. The same synthesis procedure was followed for the synthesis of $NiO@Ti_3C_2$ and $ZnO@Ti_3C_2$.

Preparation of PVA/H_2SO_4 gel electrolyte

A translucent, clear solution was obtained by heating 15 mL of 1 M H_2SO_4 solution containing 1.2 g of PVA powder in a water bath at 80 °C while stirring vigorously. Then, to remove any bubbles and create a uniform dispersion, the solution was ultrasonically treated. The resulting gel was stored at room temperature for 5 h. Finally, a PVA/H_2SO_4 polymer gel electrolyte was obtained [38].

Fabrication of $Fe_2O_3@Ti_3C_2$ electrode

A few drops of NMP were combined with the active material, which consisted of 90% $Fe_2O_3@Ti_3C_2$ and 10% carbon black. With no binders, the resulting slurry was applied using the doctor blade technique to the flexible carbon cloth. The $Fe_2O_3@$ Ti_3C_2 electrode was then prepared and dried overnight in a vacuum oven. The asymmetric flexible supercapacitor was assembled with the as-fabricated Fe_2O_3@ Ti_3C_2 as anode along with Ti_3C_2 as cathode, separated by a porous membrane and filled with PVA/H_2SO_4 polymer gel as electrolyte.

Materials characterization

Powder X-ray diffraction (XRD) was used to characterize the produced materials using a Rigaku SmartLab 3 kW equipped with an accelerator detector (Cu-Ka radiation, λ = 1.5418 Å). Using a 532 nm laser and a Witec Alpha 300 R Raman spectrometer, the Raman spectra were examined in the 200–3000 cm^{-1} range. MIRA with an EDX detector (MIRA3 XMU (MIRA-STAN)) was used to record the surface morphologies and associated elemental mapping. Brunauer-Emmett-Teller (BET, Quanta chrome instrument) method. A Kratos Analytical Axis Supra X-ray photoelectron spectrometer (XPS) with a monochromatic Al Kα (1486 eV) excitation source, was used to investigate surface chemical compositions. Each XPS spectrum was fitted using Casa XPS software, which is consistent with the C 1 s peak at 284 eV.

Electrochemical analysis

Using an electrochemical workstation (Autolab) and data analyzer powered by Nova 2.1 software, electrochemical measurements of the manufactured asymmetric flexible supercapacitor were examined using cyclic voltammetry (CV), galvanostatic charge–discharge (GCD), and electrochemical impedance spectroscopy (EIS). CV and GCD were recorded at different scan rates and current densities.

Using Eq. (1), the specific capacitance (C_{sp}, Fg^{-1})[39] was computed:

$$C_{sp} = 4 \times \frac{I\Delta t}{m\Delta V} \tag{1}$$

The following Eqs. (2) and (3) were used to compute the energy density (E, Wh kg^{-1}) and the power density (P, W kg^{-1}), respectively:

$$E = \frac{C_{sp(\Delta V)^2}}{8} \tag{2}$$

$$P = \frac{E}{\Delta t} \tag{3}$$

where m is the total mass of the two electrodes (g), ΔV is the potential window (V), I is the current density (A), and Δt is the discharging time (s).

To depict the energy storage kinetics, a power law equation was employed, as presented in the Eqs. (4) and (5).

$$\mathrm{i} = \mathrm{a}\gamma^{\mathrm{b}} \tag{4}$$

$$\log \mathrm{i} = \mathrm{b} \log \gamma + \log \mathrm{a} \tag{5}$$

The current values (i) were measured in mA, but a and b were arbitrary parameters that were derived from the slope of a linearly fitted line between log i and log v. A surface-controlled process occurs at b = 1, while a non-capacitive diffusion-controlled process occurs at b = 0.5.

Dunn's approach was applied and assessed using Eq. (6) to determine the contribution of capacitive and diffusion processes from the CV curve.

$$\mathrm{i} = \mathrm{k}_1 + \mathrm{k}_2\gamma^{\frac{1}{2}} \tag{6}$$

While "k_1" and "k_2" are constants, "i" and "v" stand for the peak current in milliamperes (mA) and the scanning rate in millivolts per second, respectively.

Data availability

The data that support the findings of this study are available from the corresponding author upon reasonable request.

Received: 9 February 2025; Accepted: 16 September 2025;

References

1. Vashishth, E. et al. Waste-cotton-cloth-derived sustainable and flexible high-performance supercapacitor. *ACS Sustain. Resour. Manag.* **1**, 548–562 (2024).
2. Yue, Y. et al. Nitrogen-doped hierarchical porous carbon films derived from metal–organic framework/cotton composite fabrics as freestanding electrodes for flexible supercapacitors. *ACS Appl. Electron Mater.* **3**, 2178–2186 (2021).
3. Liu, Y. et al. Surface structure construction of fibers in a conductive metal–organic framework/metal/cotton electrode for flexible textile supercapacitors. *ACS Appl. Electron Mater.* **4**, 4595–4604 (2022).
4. Shen, C. et al. Ultrathin coaxial fiber supercapacitors achieving high energy and power densities. *ACS Appl. Mater. Interfaces* **9**, 39391–39398 (2017).
5. Nargatti, K. I. et al. Graphene-based inks for flexible supercapacitor electrodes: a review. *ACS Appl. Electron Mater.* **6**, 24–46 (2024).
6. Arya, S. S. et al. The convergence of traditional and digital biomarkers through AI-assisted biosensing: a new era in translational diagnostics?. *Biosens. Bioelectron.* **235**, 115387 (2023).
7. Liu, Q. et al. Elucidating Li-ion adsorption and diffusion behavior on the surface of $Cu_{0.7}Co_{2.3}O_4$ and improvement of performance as flexible full solid-state supercapacitor. *Electrochim. Acta* **293**, 380–389 (2019).
8. Kumar, K. et al. Empowering energy storage technology: recent breakthroughs and advancement in sodium-ion batteries. *ACS Appl. Energy Mater.* **7**, 3523–3539 (2024).
9. Wang, B. et al. Mechanically flexible conductors for stretchable and wearable E-skin and E-textile devices. *Adv. Mater.* **31**, 1901408 (2019).
10. Xiao, Z. et al. Implementation of high-capacity 3D Ti_3C_2TX MXene supercapacitors with terminal group modification. *ACS Appl Mater. Interfaces* **15**, 51151–51159 (2023).
11. Fan, Y. et al. Patterned micro flexible supercapacitors based on the rapid transfer-printing method. *ACS Appl. Mater. Interfaces* **16**, 28780–28790 (2024).
12. Murali, G. et al. A review on MXene synthesis, stability, and photocatalytic applications. *ACS Nano* **16**, 13370–13429 (2022).
13. Kumar, Y. A. et al. 2D MXene-based supercapacitors: a promising path towards high-performance energy storage. *J. Energy Storage* **72**, 108433 (2023).
14. Gao, Y. et al. Electrochemical performance of Ti_3C_2 supercapacitors in KOH electrolyte. *J. Adv. Ceram.* **4**, 130–134 (2015).
15. Rakhi, R. B. et al. Effect of postetch annealing gas composition on the structural and electrochemical properties of Ti_2CT_x MXene electrodes for supercapacitor applications. *Chem. Mater.* **27**, 5314–5323 (2015).
16. Lukatskaya, M. R. et al. Cation intercalation and high volumetric capacitance of two-dimensional titanium carbide. *Science* **341**, 1502–1505 (2013).
17. Young, C. et al. Synergistic charge storage enhancement in supercapacitors via $Ti_3C_2T_x$ MXene and $CoMoO_4$ nanoparticles. *Micromachines* **15**, 234 (2024).
18. Prasankumar, T. et al. Advancements and approaches in developing MXene-based hybrid composites for improved supercapacitor electrodes. *Mater. Today Sustain.* **28**, 100963 (2024).
19. Vigneshwaran, J. et al. Flexible quasi-solid-state supercapacitors based on Ti_3C_2-polypyrrole nanocomposites. *Electrochim. Acta* **429**, 141051 (2022).
20. Prasankumar, T. et al. Synthesis and enhanced electrochemical performance of PANI/Fe_3O_4 nanocomposite as supercapacitor electrode. *J. Alloy. Compd.* **757**, 466–475 (2018).
21. Devi, R. K. et al. A facile strategy for the synthesis of manganese-doped nickel sulfide nanosheets and oxygen, nitrogen-enriched 3D-

graphene-like porous carbon for hybrid supercapacitor. *J. Alloy. Compd.* **944**, 169261 (2023).

22. Luo, Q. et al. Synthesis of ZnO tetrapods for high-performance supercapacitor applications. *Mater. Lett.* **198**, 192–195 (2017).
23. Ali, A. et al. Mo-doped ZnO nanoflakes on Ni-foam for asymmetric supercapacitor applications. *RSC Adv.* **9**, 27432–27438 (2019).
24. Lu, P. A. et al. Synthesis, analysis and characterization of alpha-Fe_2O_3 nanoparticles and their applications in supercapacitors. *J. Mater. Sci. Mater. Electron.* **34**, 826 (2023).
25. Gunasekaran, S. S. et al. Phytogenic generation of NiO nanoparticles as green-electrode material for high performance asymmetric supercapacitor applications. *J. Energy Storage* **37**, 102412 (2021).
26. Han, R. et al. 1D magnetic materials of Fe_3O_4 and Fe with high performance of microwave absorption fabricated by electrospinning method. *Sci. Rep.* **4**, 7493 (2014).
27. Das, R. et al. Magnetic vortex and hyperthermia suppression in multigrain iron oxide nanorings. *Appl. Sci.* **10**, 787 (2020).
28. Chen, W. et al. A MXene-based multiple catalyst for highly efficient photocatalytic removal of nitrate. *Environ. Sci. Pollut. Res.* **29**, 58149–58160 (2022).
29. Mathew, S. et al. MnO_2 anchored N–Ti_3C_2 MXene as a bifunctional electrode for enhanced water splitting. *Int. J. Hydrog. Energy* **71**, 1283–1292 (2024).
30. Deshmukh, S. et al. Laser-induced MXene-functionalized graphene nanoarchitectonics-based microsupercapacitor for health monitoring application. *ACS Nano* **17**, 20537–20550 (2023).
31. Ahmmad, B. et al. Synthesis of mesoporous hematite (α-Fe_2O_3) nanoparticles and their photocatalytic activity. *Adv. Powder Technol.* **24**, 160–167 (2013).
32. Han, T. et al. Hydrothermal self-assembly of α-Fe_2O_3 nanorings@ graphene aerogel composites for enhanced Li storage performance. *J. Mater. Sci.* **54**, 7119–7130 (2019).
33. Bhanuse, G. B. et al. Nanostructured $ZnCo_2O_4$@NiMn-LDH electrodes for supercapacitor and zinc-air battery application. *ACS Appl Nano Mater.* **7**, 13649–13663 (2024).
34. Isci, R. et al. Thienothiophene and single wall carbon nanotube-based supercapacitor as a free-standing and flexible hybrid energy storage material. *ACS Appl. Energy Mater.* **7**, 1488–1494 (2024).
35. Mondal, D. et al. Rare Earth ion-doped α-MnO_2 nanorods for an asymmetric supercapacitor. *ACS Appl. Nano Mater.* **7**, 4913–4926 (2024).
36. Liu, L. et al. Exfoliation and delamination of Ti_3C_2Tx MXene prepared via molten salt etching route. *ACS Nano* **16**, 111–118 (2022).
37. Lassoued, A. et al. Control of the shape and size of iron oxide (α-Fe_2O_3) nanoparticles synthesized through the chemical precipitation method. *Results Phys.* **7**, 3007–3015 (2017).
38. D'Altri, G. et al. Preparation and characterization of self-healing PVA–H_2SO_4 hydrogel for flexible energy storage. *ACS Omega* **9**, 6391–6402 (2024).
39. Manoharan, K. et al. Ultrasonic assisted highly porous PPy/JSAC/IMO [PJ-IMO] nanocomposite for hydrogen fuel cell and asymmetric supercapacitor (PJ-IMO||JSAC) applications. *J. Energy Storage* **70**, 107931 (2023).

Acknowledgements

This project was supported by ERDF/ESF project TECHSCALE (No. CZ.02.01.01/00/22_008/0004587). This research was co-funded by the European Union under the REFRESH - Research Excellence For REgion Sustainability and High-tech Industries project number CZ.10.03.01/00/22_003/0000048 via the environment Programme Just Transition. M.P. & K.M. acknowledges funding via project ANGSTROM. Project ANGSTROM was selected in the Joint Transnational Call 2023 of M-ERA.NET 3, which is an EU-funded network of 49 funding organisations (Horizon 2020 grant agreement No 958174). This project "Advancing Supercapacitors with Plasma-designed Multifunctional Hybrid Materials" (ANGSTROM; no. TQ05000001) is co-financed from the state budget by the Technology Agency of the Czech Republic under the SIGMA Programme within the M-ERA-NET 3 Call 2023. This project/result was funded under the National Recovery Plan from the European Recovery and Resilience Facility. K.M. would like to acknowledge Dr. Bindu Kalleshappa for technical discussions and for reviewing the manuscript. Thanks to Dr. Keval Sonigara for his suggestions for the health monitoring device measurements and Dr. Sagar Arya for giving ideas for schematic diagrams.

Author contributions

Both M.P. and K.M. conceptualized and designed the idea. K.M. prepared the materials, executed the experiments, and characterized the material. M.P. supervised the work and reviewed the manuscript. The manuscript was written through the contributions of the authors. Both authors have approved the final version of the manuscript.

Competing interests

The authors declare no competing interests.

Additional information

Supplementary information The online version contains supplementary material available at https://doi.org/10.1038/s41528-025-00489-2.

Correspondence and requests for materials should be addressed to Martin Pumera.

Reprints and permissions information is available at http://www.nature.com/reprints